

Generalized Analysis of Systems Based on Two Nonlinear Resonators

Almudena Suárez¹, Fellow, IEEE, and Franco Ramírez¹, Senior Member, IEEE

Abstract—Circuits containing two nonlinear resonators have been recently proposed for a variety of applications, such as nonlinear isolators, robust wireless power transfer, and sensors. However, their simulation is difficult due to the presence of hysteresis phenomena, associated with turning points in the solution curve, and even disconnected curves, as will be shown in this work. Here, we will present a general analysis methodology, compatible with commercial harmonic balance (HB) and able to provide all the coexisting periodic solutions. It is based on the use of two auxiliary generators (AGs), one per nonlinear resonator. The first AG acts like an independent source and controls the second one, which also depends on the input source, unlike a previously presented formulation. This extra dependence enables a systematic and broad-scope application but demands a conceptually different analysis strategy, presented in this work. Besides its numerical capabilities (in combination with HB), the new formulation will provide insight into the complex behavior of systems composed by two nonlinear resonators. It will be illustrated through its application to a Lorentzian–Fano nonlinear isolator and a system for robust near-field wireless power transfer, in which the new formulation particularizes to the previous one.

Index Terms—Auxiliary generators (AGs), contour intersections, hysteresis, nonlinear resonators.

I. INTRODUCTION

HYSTERESIS phenomena versus the input power and other parameters are intrinsic to the behavior of nonlinear resonators [1], [2], [3], [4], [5], [6], [7]. This hysteresis is associated with the coexistence of periodic steady-state solutions in some parameter intervals, delimited by turning points, at which the slope of the solution curve tends to infinite. When using harmonic balance (HB), the Jacobian matrix of the HB system becomes singular at the turning points [8], [9], [10]. Moreover, an ill-conditioning problem is often observed before reaching the turning point, which may lead to convergence failures or to a jump to a coexisting solution. To obtain the complete solution curve in in-house HB, one should make use of continuation methods such as parameter

switching [11] or arc length [12]. Basically, these methods replace the actual physical parameter (such as the input power) with a parameter versus which the circuit/system does not exhibit the turning point. In the case of commercial HB, manual parameter switching can be carried out by introducing an auxiliary generator (AG) [13], [14] into the circuit. The voltage (current) AG must satisfy a nonperturbation condition given by the zero value of the ratio between its current and voltage (voltage and current) [15], which provides an outer tier equation, solved through optimization [13], [14]. In the case of nonautonomous circuits (such as a nonlinear resonator), the outer tier variables are the AG amplitude and phase. Thus, depending on the section of the solution curve, we will sweep the physical parameter or the AG amplitude or phase. This switching is manual and involves a sequence of parameter changes and sweeps that will become cumbersome in the case of intricate curves. Recently, a new contour method [16], [17], [18], compatible with commercial HB, has been proposed. It also relies on the introduction into the circuit of an AG, which unlike [13] and [14] is not optimized. Instead, it is used to calculate a nonlinear immittance (admittance or impedance) function in commercial HB. This function depends on the excitation amplitude and frequency, in the case of an autonomous circuit, or amplitude and phase, in a nonautonomous one. It allows obtaining the solution curves either as contour levels [16], [17], directly traced in commercial HB, or by calculating contour intersections [18] in in-house software. The method takes advantage of the fact that the direct excitation of the nonlinear device at the fundamental frequency rarely gives rise to convergence problems. This is because the device nonlinearities are not multivalued in terms of their time-domain control voltages. In the presence of disconnected solution curves, the method is also advantageous with respect to in-house software. This is because it exhaustively (and simultaneously) provides all the solutions coexisting for a given parameter value, which may belong to different sections of the same curve or even to different curves.

The method (based on the calculation of a *single* nonlinear immittance function) is applicable to a complete transistor, due to the compacity of its nonlinear core. However, in circuits in which the nonlinearities are not closely connected, the procedure fails. This is the case of circuits containing two nonlinear resonators, which have recently attracted interest for a variety of applications, including nonlinear isolators [19], [20], [21], [22], [23], robust wireless power transfer [24], [25], and sensors [26], [27], [28], [29], [30], [31]. The multivalued solution may originate in either one or another resonator or

Manuscript received 14 July 2023; revised 28 September 2023; accepted 28 October 2023. This work was supported by the Spanish Ministry of Science and Innovation (MCIN/AEI/10.13039/501100011033) under Grant PID2020-116569RB-C31 and Gobierno de Cantabria (Contrato Programa Gobierno de Cantabria—UC). This article was presented at the IEEE MTT-S International Microwave Symposium (IMS 2023), San Diego, CA, USA, June 11–16, 2023 [DOI: 10.1109/LMWT.2023.3264991]. (Corresponding author: Franco Ramírez.)

The authors are with the Departamento de Ingeniería de Comunicaciones, Universidad de Cantabria, 39005 Santander, Spain (e-mail: almudena.suarez@unican.es; ramirezf@unican.es).

Color versions of one or more figures in this article are available at <https://doi.org/10.1109/TMTT.2023.3329734>.

Digital Object Identifier 10.1109/TMTT.2023.3329734

be the result of the combined action of both. Thus, two AGs, one per nonlinear resonator, would be needed, each with its own amplitude and phase, making a total of *four* independent outer tier values. As a result, the contour methods in [16], [17], and [18], valid only with two independent variables, are not applicable.

Here, we will present a general analysis methodology for circuits with two nonlinear resonators, compatible with commercial HB and able to provide all the coexisting periodic solutions. It is also based on the use of two AGs, one per nonlinear resonator. However, one AG (AG2) depends on the other (AG1) [32], which allows limiting the number of outer tier variables to two variables instead of four variables and a single outer tier (complex) equation instead of two, thus enabling the application of the exhaustive contour procedures. Here, we will generalize the formulation in [32] by considering the dependence of AG1 on the AG2 voltage and the input (external) source. This extra dependence enables a systematic and broad-scope application but demands a conceptually different analysis strategy. Besides the two AGs, the implementation procedure requires certain complementary elements and functions that will be described here in full detail.

Besides its numerical capabilities (in combination with HB), the new formulation provides insight into the complex behavior of systems containing nonlinear resonators, as will be demonstrated here with two different examples. It will be initially applied to a Fano nonlinear isolator [19], [20], which will enable a circuit-level understanding of the mechanism for the nonreciprocal behavior. It will also enable an analytical quantification of the differences in the power-transfer response when driving the system in forward and backward sense. Then, we will address the more complex Lorentzian–Fano nonlinear isolator [19], [20], [21], [22], [23]; by means of the new formulation, we will identify the qualitative differences with the Fano isolator, resulting from the combined action of its two nonlinear resonators. We will also investigate the system based on two coupled nonlinear resonators that were proposed in [24] and [25] for a robust near-field wireless power transfer. When applied to this system, the new formulation particularizes to the one in [32]. With the aid of the formulation, it will be possible to identify the mechanism that, for a given driving power, enables a significant increase of the distance between the coils. In the two cases, the results of the new formulation will be validated with default and optimization-based HB (when convergence is achieved) and with experimental measurements.

This article is organized as follows. Section II presents the generalized formulation of systems containing two nonlinear resonators. It includes a detailed description of its implementation on commercial HB, as well as its particularization to formulation in [32]. Section III describes its application to the analysis of a Lorentzian–Fano nonlinear isolator. Finally, Section IV describes its application to a robust near-field wireless-power-transfer system.

II. GENERALIZED FORMULATION OF SYSTEMS CONTAINING TWO NONLINEAR RESONATORS

For the generalized analysis, we will consider the system in Fig. 1(a), which contains two nonlinear elements

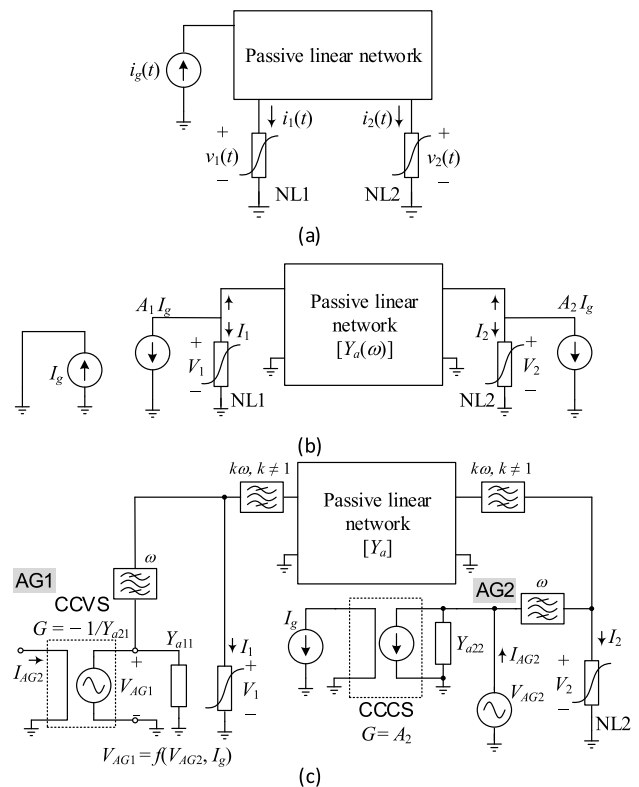


Fig. 1. Analysis of the circuit with two linear elements NL1 and NL2. (a) General block diagram considered for the piecewise-type HB formulation in (1). (b) General circuit described with the equation system (2), at the fundamental frequency. (c) Setup used for the calculation of the error function $H(V_{AG2}, \phi)$ defined in (8). Due to the action of the ideal bandpass filters, one has a schematic containing the AGs at the fundamental frequency and the original circuit schematic at the rest of harmonic terms.

(NL1 and NL2), an arbitrary passive-linear embedding network, and an input source I_g . We will first derive the formulation that enables the new analysis method, based on the use two AGs. Then, we will present the implementation on HB and the particularization to the formulation in [32].

A. Calculation of the Steady-State Solutions

For a description of the procedure, we will assume a periodic solution at the input-source frequency ω and a piecewise HB formulation of the type in [33], [34], and [35]. Thus, the system can be described as

$$\begin{bmatrix} V_{1,k} \\ V_{2,k} \end{bmatrix} + \begin{bmatrix} Z_{a11}(k\omega) & Z_{a12}(k\omega) \\ Z_{a21}(k\omega) & Z_{a22}(k\omega) \end{bmatrix} \begin{bmatrix} I_{1,k}(\bar{V}_1, \omega) \\ I_{2,k}(\bar{V}_2, \omega) \end{bmatrix} + \begin{bmatrix} Z_{g1}(k\omega) \\ Z_{g2}(k\omega) \end{bmatrix} I_{g,k} = 0 \quad (1)$$

where k is the harmonic index, $V_{1,k}$ and $V_{2,k}$ are the k th harmonic components of the voltages $[v_1(t)$ and $v_2(t)]$ across the two nonlinear elements NL1 and NL2, respectively, $I_{1,k}$ and $I_{2,k}$ are the harmonic components of the currents $[i_1(t)$ and $i_2(t)]$ entering these elements, and $I_{g,k}$ are the harmonic components of the input current, equal to zero for $k \neq \pm 1$. On the other hand, \bar{V}_i , where $i = 1, 2$, is the vector containing the whole set of harmonics of $v_1(t)$ and $v_2(t)$. Finally, $[Z_{aij}]$ is the linear impedance matrix that relates $V_{1,k}$ and $V_{2,k}$

to $I_{1,k}$ and $I_{2,k}$ when doing $I_g = 0$, and $[Z_{gi}]$ is the linear column matrix that relates $V_{1,k}$ and $V_{2,k}$ to $I_{g,k}$ when doing $I_{1,k} = I_{2,k} = 0$.

The analysis method requires a special treatment of the subsystem of (1) at the fundamental frequency ω since the two AGs operate at this frequency. At the harmonic frequencies, we will consider the original circuit schematic [Fig. 1(a)]. When using commercial HB, the different treatments at ω and the harmonic components are enabled by the introduction of ideal filters. In all cases of practical interest, the 2×2 impedance matrix $[Z_{aij}(\omega)]$ will be invertible. Multiplying the two terms of (1) by the admittance matrix $[Y_{aij}(\omega)] = [Z_{aij}(\omega)]^{-1}$, one obtains

$$\begin{aligned} Y_{a11}V_1 + Y_{a12}V_2 + I_1(\bar{V}_1) + A_1I_g &= 0 \quad (\text{a}) \\ Y_{a21}V_1 + Y_{a22}V_2 + I_2(\bar{V}_2) + A_2I_g &= 0 \quad (\text{b}) \end{aligned} \quad (2)$$

where for simplicity, we do not explicitly show the harmonic index $k = 1$ and the dependence on ω . We have also defined

$$\begin{aligned} A_1 &= Y_{a11}Z_{g1} + Y_{a12}Z_{g2} \\ A_2 &= Y_{a21}Z_{g1} + Y_{a22}Z_{g2}. \end{aligned} \quad (3)$$

Unlike (1), the two complex equations of (2) depend each on a single nonlinear current I_i ($i = 1, 2$). Following (2), the circuit can be represented with the schematic in Fig. 1(b). Now, we can solve (2)(b) for V_1 , which provides

$$V_1 = \frac{-Y_{a22}V_2 - I_2(\bar{V}_2) - A_2I_g}{Y_{a21}}. \quad (4)$$

With the above derivation, V_1 depends on both \bar{V}_2 and the input current I_g , unlike the expression in [32]. Instead, the one in [32] provides a less general relationship, in which V_1 does not depend on I_g . As a result, it may fail under certain operation conditions, as will be shown in the application examples.

The relationship (4) will be used to obtain a single outer tier equation depending on two real state variables only. This will be achieved by making use of two voltage AGs, which will be independent and dependent. The independent voltage AG (AG2) is connected in parallel with the second nonlinear element, as shown in Fig. 1(c). Note that due to the ideal filters in the schematic, it only has an effect at the fundamental frequency. At the rest of harmonic frequencies, the circuit fully agrees with the original one. At the fundamental frequency, AG2 will play the role of V_2 , so we can write

$$\begin{aligned} V_{AG2} &= V_2, \\ V_{AG2} &= |V_{AG2}|e^{j0}. \end{aligned} \quad (5)$$

Note that we have arbitrarily imposed a zero-phase value to AG2 and, thus, we set the phase origin at V_2 . From Fig. 1(c), the current flowing up AG2 is

$$I_{AG2} = Y_{a22}|V_{AG2}| + I_2(|V_{AG2}|) + A_2|I_g|e^{j\phi} \quad (6)$$

where I_2 also depends on the Fourier coefficients $k \neq 1$ of $v_2(t)$, which is not shown for notation simplicity. Because we have set the phase origin at $V_2 = |V_{AG2}|$, the input current I_g is expressed in terms of its amplitude $|I_g|$ and its phase

shift ϕ with respect to V_2 . Next, we will apply (4) to obtain the value of the second voltage AG (AG1). Replacing (5) in (4)

$$V_{AG1}(|V_{AG2}|, |I_g|e^{j\phi}) = \frac{-I_{AG2}(|V_{AG2}|, |I_g|e^{j\phi})}{Y_{a21}}. \quad (7)$$

The voltage V_{AG1} depends on the current I_{AG2} , which in turn depends on the control voltage V_{AG2} [and all the harmonic terms of $v_2(t)$] and the input generator I_g . Note that V_{AG1} is a complex variable. Due to the filters in Fig. 1(c), AG1 only has an effect at the fundamental frequency, in a manner like AG2. Using AG1 and AG2 [Fig. 1(c)], we are directly controlling the two nonlinear elements NL1 and NL2 at the fundamental frequency, which will necessarily limit the convergence problems associated with turning points.

Once we have the values of the two AGs, we will make use of (2)(a) to obtain a single outer tier equation in terms of the independent voltage $V_2 = V_{AG2} = |V_{AG2}|e^{j0}$ and $|I_g|e^{j\phi}$. This is given by

$$\begin{aligned} H(|V_{AG2}|, \phi) &= Y_{a11}V_{AG1}(|V_{AG2}|, |I_g|e^{j\phi}) + Y_{a12}|V_{AG2}| \\ &\quad + I_1(V_{AG1}) + A_1|I_g|e^{j\phi} = 0 \end{aligned} \quad (8)$$

where the dependences on Fourier components $k \neq 1$ are not shown for simplicity. The complex equation (8), in the two state variables: $|V_{AG2}|, \phi$, constitutes an outer tier equation, whereas the pure HB system, with as many harmonic terms as required, acts like an inner tier. To obtain the circuit solutions, we will first perform a double sweep in $|V_{AG2}|, \phi$ to calculate the functions

$$\begin{aligned} H_r(|V_{AG2}|, \phi) &= \text{Re}[H(|V_{AG2}|, \phi)] \\ H_i(|V_{AG2}|, \phi) &= \text{Im}[H(|V_{AG2}|, \phi)]. \end{aligned} \quad (9)$$

Then, all the solutions in the considered exploration plane (defined by $0 < |V_{AG2}| \leq |V_{AG2,\max}|$ and $0 < \phi \leq 2\pi$) are given by the *intersections* of the two following contours:

$$\begin{aligned} H_r(|V_{AG2}|, \phi) &= 0 \\ H_i(|V_{AG2}|, \phi) &= 0 \end{aligned} \quad (10)$$

where the subscripts r and i indicate real and imaginary parts, respectively. Multivalued solution curves versus any arbitrary parameter η , such as the input current $|I_g|$ or frequency ω , are obtained by representing all the intersection points versus η .

B. Implementation on Commercial HB

For the implementation on commercial HB, we make use of the schematic of Fig. 1(c), with the represented ideal filters. At the harmonic terms $k\omega$ with $k \neq 1$, we have the original circuit with all its elements and connections. At the fundamental frequency ω , we must introduce the two AGs shown in Fig. 1(c) and make use of the passive-linear matrix $[Y_a]$ and the parameters A_i , where $i = 1, 2$. Both $[Y_a]$ and A_i are obtained from previous (undemanding) analyses of the passive-linear network. At the fundamental frequency ω , together with AG2, we have [on the right of Fig. 1(c)] the parallel connection of the nonlinear element NL2, the passive-linear admittance one-port block Y_{a22} , and a current-controlled current source (CCCS) with the value $A_2|I_g|e^{j\phi}$. By Kirchoff's laws, the current flowing up AG2 is given by (6). Then, from (7),

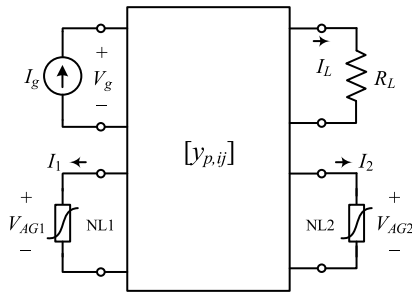


Fig. 2. Four-port block, described with the linear admittance matrix $[y_{p,ij}]$, used for the calculation of the output power.

the voltage V_1 should be: $V_1 = -Y_{a21}^{-1}I_{AG2}$. This is imposed with AG1, which has the complex value $V_{AG1} = -Y_{a21}^{-1}I_{AG2}$ and is connected in parallel with NL1, as shown on the left of Fig. 1(c). Then, we introduce the error function (8) as an equation in the data display window. Under a given input amplitude $|I_g|$, to obtain the solution curve (or curves) versus a parameter η , we perform, for each η , a double sweep in $|V_{AG2}|$ and ϕ , and obtain the intersections between the two contours $Re[H(|V_{AG2}|, \phi)] = 0$ and $Im[H(|V_{AG2}|, \phi)] = 0$. The parameter η may be $|I_g|$, the input frequency ω , or an arbitrary circuit element. These intersections are calculated in in-house software after exporting the functions $Re[H(|V_{AG2}|, \phi)] = 0$ and $Im[H(|V_{AG2}|, \phi)] = 0$ from commercial HB.

C. Calculation of Insertion Loss/Isolation

Once we have obtained the steady-state solutions of (8) in terms of V_{AG1} [from (7)] and V_{AG2} , the variables at the input–output ports (at the fundamental frequency ω) are calculated considering the four-port passive-linear network that connects the two nonlinear elements (NL1 and NL2), the input generator I_g , and the output load resistor R (Fig. 2). Using the four-port admittance matrix $[y_{p,ij}]$, one obtains the following linear system:

$$\begin{aligned} I_g &= y_{p,11}V_g + y_{p,12}V_{AG1} + y_{p,13}V_{AG2} + y_{p,14}R_L I_L \\ -I_1 &= y_{p,21}V_g + y_{p,22}V_{AG1} + y_{p,23}V_{AG2} + y_{p,24}R_L I_L \\ -I_2 &= y_{p,31}V_g + y_{p,32}V_{AG1} + y_{p,33}V_{AG2} + y_{p,34}R_L I_L \\ -I_L &= y_{p,41}V_g + y_{p,42}V_{AG1} + y_{p,43}V_{AG2} + y_{p,44}R_L I_L. \end{aligned} \quad (11)$$

Note that all the variables in (11) are known except the load current I_L and the voltage at the input source V_g . This is because the steady-state analysis in Section II-B provides $I_g, V_{AG1}, V_{AG2}, I_1$, and I_2 . To calculate the output power, one will simply obtain I_L from any two equations of (11), providing a nonsingular 2×2 system. Then, the ratio between the output power and the available power is

$$T = \frac{\frac{1}{2}R_L |I_L|^2}{\frac{|I_g|^2}{8G}} = \frac{4GR_L |I_L|^2}{|I_g|^2} \quad (12)$$

which agrees with the inverse of the transmission loss. In a more general way, to obtain a given harmonic component of any variable, one should extract it from commercial HB and apply interpolation to obtain its value at each contour intersection.

D. Particular Case [32]

Depending on the network topology, we can have a simpler situation in which the current through the first nonlinear element (NL1) does not directly depend on I_g . This is the case considered in [32]. Under this assumption, (2) simplifies to

$$\begin{aligned} Y_{a11}V_1 + Y_{a12}V_2 + I_1(\bar{V}_1) + A_1 I_g &= 0 \quad (a) \\ Y_{a21}V_1 + Y_{a22}V_2 + I_2(\bar{V}_2) &= 0 \quad (b). \end{aligned} \quad (13)$$

Thus, we have the AG values

$$\begin{aligned} V_{AG2} &= |V_{AG2}|e^{j\phi} \\ V_{AG1}(|V_{AG2}|) &= \frac{-Y_{a22}|V_{AG2}| - I_2(|V_{AG2}|)}{Y_{a21}} \end{aligned} \quad (14)$$

where V_{AG1} has been calculated from (13)(b). Again, the dependences on the harmonic terms and ω have been omitted for simplicity. Replacing both expressions in (13)(a), we get

$$\begin{aligned} Y_{a11} \frac{-Y_{a22}|V_{AG2}| - I_2(|V_{AG2}|)}{Y_{a21}} + Y_{a12}|V_{AG2}| \\ + I_1(|V_{AG2}|, \omega) + A_1 |I_g|e^{j\phi} &= 0. \end{aligned} \quad (15)$$

The above equation can be rewritten in terms of a function, $H_p(|V_{AG2}|)$, that does not depend on the input current I_g , by doing

$$\begin{aligned} H_p(|V_{AG2}|) &= Y_{a11}V_{AG1}(|V_{AG2}|) + Y_{a12}|V_{AG2}| + I_1(V_{AG1}) \\ &= -A_1 |I_g|e^{j\phi}. \end{aligned} \quad (16)$$

Under a given input amplitude $|I_g|$, to obtain the solution curve (or curves) versus a parameter η , we perform a double sweep in η and V_{AG2} and simply trace the contour $|H_p(\eta, |V_{AG2}|)| = |I_g|$ in the plane $|V_{AG2}|, \eta$. One advantage is that we can obtain the solution curve (or curves) in commercial HB through simple contour tracing. Another advantage is that we can get the complete family of solution curves V_{AG2} versus η for different $|I_g|$ values with no need to sweep $|I_g|$. This is because these curves agree with the contour plots of $|H_p(\eta, |V_{AG2}|)|$. As stated, the disadvantage is that this method is not general.

Note that it is possible to know in advance if (16) can be used. We must directly excite NL1 and NL2 with the two AGs. In these conditions, to use (16), the voltage at NL1 (V_1) must only depend on the voltage (V_2) and current (I_2) at NL2. This implies a coefficient $A_2 = 0$ in system (2). Thus, the voltage V_1 must be fully determined by V_2, I_2 , and the admittance matrix $[Y_{aij}(\omega)]$. If this is not the case, we must apply the new method based on the general formulation (8).

To summarize, the main advantage of the new methods is their systematic nature, just based on either two or three nested sweeps carried out in commercial HB, to obtain a nonlinear function, H_p or H . In comparison, the AG optimization [10], [37], [38] requires the user surveillance of the convergence process and a manual parameter switch when this convergence fails. Moreover, the optimization and parameter switching are not exhaustive and can miss solution curves. This is also true for in-house HB combined with continuation procedures. In comparison, the new method enables a global search for solutions in the exploration space, comprised within the limits of the sweep intervals. Table I presents a comparison with the existing HB-based methods to trace multivalued curves.

TABLE I
COMPARISON OF HB-BASED METHODS TO TRACE MULTIVALUED CURVES

Method	Capability to pass through turning points	Capability to provide disconnected curves	Commercial-HB compatible	Memory usage / Simulation time	User involvement
Default HB	No	No	Yes	Low	Low
In-house HB with continuation [8],[9],[36]	Yes	No	No	Low	Low
In-house HB with AG continuation [15]	Yes	No	No	Medium	Low
Commercial HB with AG optimization [10],[37],[38]	Yes	No	Yes	Medium	High
New method	Yes	Yes	Yes	High	Low

III. LORENTZIAN–FANO NONLINEAR ISOLATOR

Sounas et al. [19], Cotrufo et al. [20], Sounas and Alù [21], Kord et al. [22], and Cotrufo et al. [23] proposed a nonreciprocal isolator based on the coupling through a transmission line of two nonlinear resonators of Lorentzian and Fano type (Fig. 3). Besides its numerical capabilities, the new formulation provides insight into the operation of this nonlinear isolator at the circuit level. For an easier understanding, the analysis will be carried out in two stages. We will first address the Fano isolator and then the Lorentzian–Fano one.

A. Fano Nonlinear Isolator

The Fano nonlinear isolator [Fig. 4(a)] will be described in terms of the admittance matrix $[y_{ij}]$, shown in Fig. 4(b) and (c), which contains the transmission line of electrical length θ and the two capacitors C_1 and C_2 . In the two senses (forward and backward), we will formulate the circuit with a single-variable version of (1). At the fundamental frequency, we have

$$V + Z_a(\omega)I(V, \omega) + Z_g(\omega)|I_g|e^{j\phi} = 0. \quad (17)$$

The above equation will now be particularized to operation in the forward and backward senses. In the forward sense, we have

$$H_f(V, \phi) = V + \left(jL_2\omega + \frac{1}{G + y_{\text{out}}} \right) I(V, \omega) + \left(\frac{y_{12}}{y_{11} + G} \right) \left(\frac{1}{G + y_{\text{out}}} \right) |I_g|e^{j\phi} = 0 \quad (18)$$

where the subscript f indicates forward, $G = R^{-1}$, and

$$y_{\text{out}} = z_{\text{out}}^{-1} = y_{22} - \frac{y_{12}y_{21}}{y_{11} + G}. \quad (19)$$

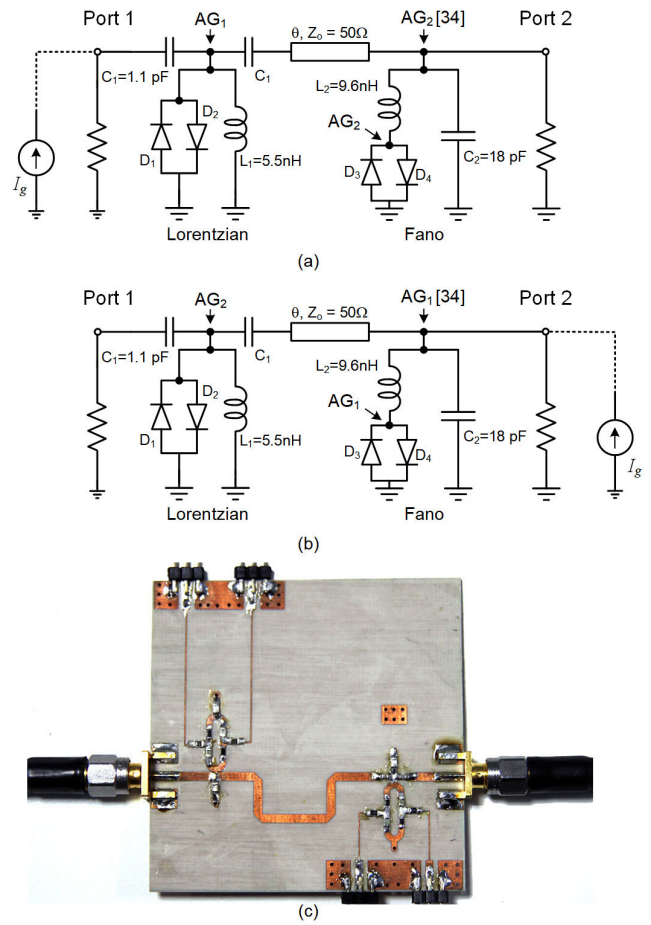


Fig. 3. Lorentzian–Fano nonlinear isolator [19], [20], [21], [22], [23]. The nonlinearities NL1 and NL2 are implemented as antiparallel connected diodes (Skyworks SMV1232). The rest of element values are shown in the figure. The connection nodes of the AGs when using the method in [32] and the new method are indicated. (a) Operation in forward sense. (b) Operation in backward sense. (c) Photograph of the measured prototype.

In the backward sense, we have

$$H_b(V, \phi) = V + \left(jL_2\omega + \frac{1}{G + y_{\text{out}}} \right) I(V, \omega) - \left(\frac{1}{G + y_{\text{out}}} \right) |I_g|e^{j\phi} = 0 \quad (20)$$

where the subscript b indicates backward.

Comparing (18) and (20), the only difference is the extra nondimensional factor $\chi = -y_{12}(y_{11} + G)^{-1}$ affecting the current I_g in the case of the forward sense [see (18)]. As a result, the curve V versus $|I_g|$ will only differ in the scaling factor $|\chi|$. The output power in the two senses is

$$P_{\text{out},f} = \frac{1}{2} \frac{|V(|I_g|) + jL_2\omega I[V(|I_g|)]|^2}{R} \quad (a)$$

$$P_{\text{out},b} = \frac{1}{2} |\chi|^2 \frac{|V(|I_g||\chi|^{-1}) + jL_2\omega I[V(|I_g||\chi|^{-1})]|^2}{R} \quad (b). \quad (21)$$

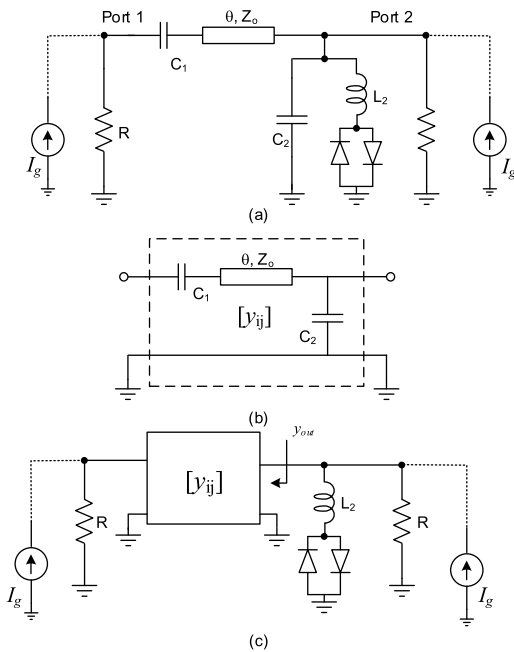


Fig. 4. Fano nonlinear isolator. (a) Schematic. (b) Admittance matrix $[y_{ij}]$ considered in the formulation. It contains the transmission line and the two capacitors C_1 and C_2 . (c) General schematic, in terms of the admittance matrix $[y_{ij}]$.

Also, the respective ratios between the output power and the available power are

$$T_f = 4 \frac{|V(|I_g|) + jL_2\omega I[V(|I_g|)]|^2}{R^2} = S(P_{dg})$$

$$T_b = 4|\chi|^2 \frac{|V(|I_g||\chi|^{-1}) + jL_2\omega I[V(|I_g||\chi|^{-1})]|^2}{R^2}$$

$$= |\chi|^2 S(P_{dg}|\chi|^{-2}). \quad (22)$$

From the inspection of (22), in the case of a linear response $I(V, \omega) = Y_{in}(\omega)V$, the network will be reciprocal since $S(P_{dg}|\chi|^{-2}) = |\chi|^{-2}S(P_{dg})$ and $T_f = T_b$. Thus, for a noticeable nonreciprocal behavior, we must fulfill two conditions. The first is the operation of the diode in a sufficiently nonlinear region to obtain a (significantly) different response of (18) and (20) under the extra factor $|\chi|^{-1}$ affecting I_g in (18). The second condition is that $|\chi|$ must be sufficiently different from 1. However, the variation of $\chi = -y_{12}(y_{11} + G)^{-1}$ will affect the power transfer; in backward sense, it will modify the output admittance $y_{out} = z_{out}^{-1} = y_{22} + \chi y_{21}$ [indicated in Fig. 4(c)]. With the required large value of $|\chi|$, one may expect a significant reduction of output power.

To validate the above derivation, we have analyzed the Fano resonator in Fig. 4 at 750 MHz, using two different sets of element values, as shown in the caption of Fig. 5. Note that for this numerical analysis, we have considered full models of the devices and passive-linear elements, including parasitics. For the case in Fig. 5(a), we have $|\chi| = 7.8$ dB. In turn, for the case in Fig. 5(b), we have $|\chi| = 1$ dB. In the two cases, we compare the power transmission in the forward and backward senses. Even though, for this analysis, we have considered full component models, the predictions of (21)–(22) keep valid, which demonstrates their generality. The results obtained with (17) are verified with default HB simulations.

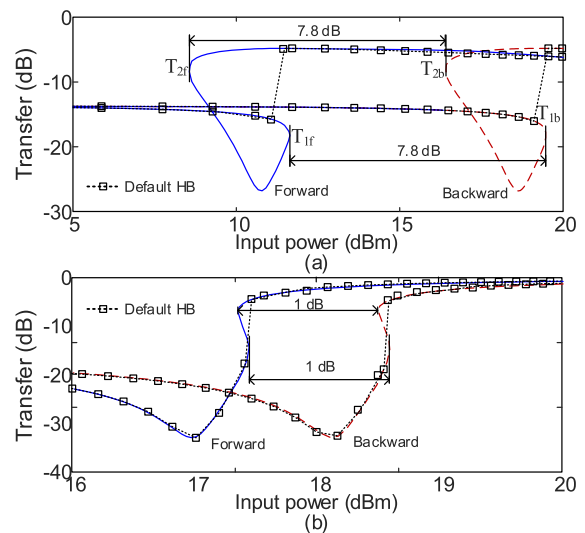


Fig. 5. Fano nonlinear isolator. Power transfer curves for two different sets of parameter values at $f_{in} = 750$ MHz. The results obtained with (17) are verified with default HB simulations (squares). (a) $C_1 = 1.1$ pF, $G = 1/50$ S, $y_{11} = 2.513 \times 10^{-4} + j0.023$ S, and $y_{12} = -0.001 - j0.076$ S, with $|\chi| = 7.8$ dB. (b) $C_1 = 11$ pF, $G = 1/50$ S, $y_{11} = 2.489 \times 10^{-5} - j0.007$ S, and $y_{12} = 2.295 \times 10^{-6} + j0.024$ S, with $|\chi| = 1$ dB.

They are overlapped except in the multivalued sections, where default HB fails to converge. A simple stability analysis through pole-zero identification [39], [40] demonstrates that in the two senses, the lower and upper sections of the solution curve are stable, whereas the section comprised between the turning points T_{1f} and T_{2f} , in the forward sense, and between T_{1b} and T_{2b} , in the backward sense, is unstable. Since $|\chi| > 1$, both the turning points and minimum of the forward curve occur for lower input power than those of the backward one (Fig. 5).

The input power (P_{in}) interval with nonreciprocal operation is comprised between T_{1f} in the forward sense (which gives rise to a transition from low power transmission to higher power transmission) and T_{1b} in the backward sense (which also gives rise to a transition to higher power transmission). As in [19], [20], [21], [22], and [23], it is assumed that the coexisting upper sections of the curves (in the nonreciprocal interval) are never reached since there is no gradual reduction of the input power.

As gathered from Fig. 5, for a stronger reciprocity, there are higher transmission losses, in consistency with the previous discussion on the impact of $|\chi|$. This agrees with the demonstration in [19] for resonators with a Kerr-type nonlinearity, using coupled-mode theory. The analysis (21) and (22), at the circuit level, enables an exact quantification of the scaling of the power-transfer curve in the backward sense, with respect to the forward one.

Crucial points of the solution curve in both the forward and backward senses (see Fig. 5 as an example) are the turning points and the transmission minima. We will first consider the turning points. The steady-state equations (18) or (20) (depending on the sense) can be rewritten as

$$H_\gamma(V, \phi) = V + \left(jL_2\omega + \frac{1}{G + y_{out}} \right) I(V, \omega) + A_\gamma |I_g| e^{j\phi}$$

$$= F(V, \omega) + A_\gamma |I_g| e^{j\phi} = 0 \quad (23)$$

where the subscript γ is f for the forward sense and b for the backward sense. At the turning points, the Jacobian matrix associated of the system composed by the real and imaginary parts of (23) becomes singular. Thus, we have the condition

$$\det \begin{bmatrix} \frac{\partial H_{\gamma,r}}{\partial V} & \frac{\partial H_{\gamma,r}}{\partial \phi} \\ \frac{\partial H_{\gamma,i}}{\partial V} & \frac{\partial H_{\gamma,i}}{\partial \phi} \end{bmatrix} = 0 \quad (24)$$

where the subscripts r and i indicate real and imaginary parts, respectively. The derivative with respect to the phase ϕ is given by

$$\frac{\partial H_{\gamma}(V, \phi)}{\partial \phi} = jA_{\gamma}|I_g|e^{j\phi} = -jF(V, \omega). \quad (25)$$

Then, the turning-point condition can be written as

$$\det \begin{bmatrix} \frac{\partial F_r}{\partial V} & F_i \\ \frac{\partial F_i}{\partial V} & -F_r \end{bmatrix} = -\frac{\partial(F^2)}{\partial V} = 0. \quad (26)$$

As gathered from (26), the voltage amplitudes V_{TP} at the turning points are the same for both the forward and backward senses since they do not depend on A_{γ} . However, and in consistency with the scaling of the power-transfer curve, the amplitude of the input current I_g at these turning points will be different and is given by

$$\begin{aligned} |I_{g,f}| &= \left| F(V_{TP}, \omega) \left(\frac{z_{out} + R}{z_{out}R} \right) \right| |\chi|^{-1(a)} \\ |I_{g,b}| &= \left| F(V_{TP}, \omega) \left(\frac{z_{out} + R}{z_{out}R} \right) \right| (b). \end{aligned} \quad (27)$$

Next, we will address the transmission minima. When neglecting the diode losses, there will be a transmission null (in both the forward and backward senses) when the condition $V + jL_2\omega I(V, \omega) = 0$ is fulfilled. In a manner like the turning points, the voltage V at the transmission null is the same in the forward and backward senses. However, as in the case of the turning points, the input current in the forward sense is scaled by $|\chi|^{-1}$. Note that in Fig. 5, the minima are not zero ($-\infty$) due to the influence of the parasitics.

B. Lorentzian–Fano Nonlinear Isolator

The Lorentzian–Fano isolator includes two nonlinear resonators (Fig. 3), which, as illustrated by the formulation, will reinforce the nonreciprocal behavior. In the forward (subscript f) and backward (subscript b) senses, the equation systems are

$$\begin{cases} H_{1f} = Y_{a11}V_1 + Y_{a12}V_2 + I_1(\bar{V}_1, \omega) + A_{1,f}I_g = 0 & (a) \\ H_{2f} = Y_{a12}V_1 + Y_{a22}V_2 + I_2(\bar{V}_2, \omega) = 0 & (b) \\ H_{1b} = Y_{a11}V_1 + Y_{a12}V_2 + I_1(\bar{V}_1, \omega) + A_{1,b}I_g = 0 & (c) \\ H_{2b} = Y_{a12}V_1 + Y_{a22}V_2 + I_2(\bar{V}_2, \omega) + A_{2,b}I_g = 0 & (d) \end{cases} \quad (28)$$

The two systems [(28)(a) and (b) and (28)(c) and (d)] are identical except for the nondimensional coefficients $A_{i,f}$

and $A_{i,b}$, where $i = 1, 2$, that affect the input current. These coefficients are

$$\begin{aligned} A_{1,f} &= -\frac{I_1}{I_g} \Big|_{V_1=V_2=0} = \frac{-1}{1 + G/(jC_1\omega)} \\ A_{2,f} &= -\frac{I_2}{I_g} \Big|_{V_1=V_2=0} = 0 \\ A_{1,b} &= \frac{-I_1}{I_g} \Big|_{V_1=V_2=0} = \frac{-\frac{1}{jL_2\omega}}{G + \frac{1}{jL_2\omega} + jC_2\omega + Y_{in}(\theta, C_1)} \\ A_{2,b} &= \frac{-I_2}{I_g} \Big|_{V_1=V_2=0} = \frac{-Y_{in}(\theta, C_1)}{G + \frac{1}{jL_2\omega} + jC_2\omega + Y_{in}(\theta, C_1)} \end{aligned} \quad (29)$$

where $Y_{in}(\theta, C_1)$ is the input admittance of the transmission line when terminated in C_1 . The lack of symmetry when exciting the system in the forward and backward senses is due to the difference between $A_{1,f}$ and $A_{i,b}$ and between Y_{a11} and Y_{a22} . However, unlike what happens with the Fano resonator, each of the two nonlinear elements, NL1 and NL2, will operate in a qualitatively different manner when exciting the system in the forward or backward senses. This can be understood from the differences in V_1 when exciting the circuit in the forward and backward senses

$$\begin{aligned} V_{1,f}(V_2, I_g) &= \frac{-Y_{a22}|V_2| - I_2(V_2, \bar{V}'_2)}{Y_{a21}} \\ V_{1,b}(V_2, I_g) &= \frac{-Y_{a22}V_2 - I_2(V_2, \bar{V}'_2) - A_{2,b}|I_g|e^{j\phi}}{Y_{a21}}. \end{aligned} \quad (30)$$

On the other hand, neglecting parasitics, the output power is

$$\begin{aligned} P_{out,f} &= \frac{1}{2} \frac{|V_2 + jL_2\omega I_2|^2}{R} \\ P_{out,b} &= \frac{1}{2} \left| \frac{1}{1 + G/(jC_1\omega)} \right|^2 \frac{|V_1|^2}{R} = \frac{1}{2} |A_{1,f}|^2 \frac{|V_1|^2}{R}. \end{aligned} \quad (31)$$

In the two senses, the transmission zeroes will be given by the condition $V_2 + jL_2\omega I_2(V_2, \omega) = 0$. This is because, under this condition, $I_g = I_2$ and $I_1 = 0$, as easily gathered from the inspection of the circuit topology. However, the above transmission zero will be reached for a different input current in each sense.

The new analysis method will be applied to the circuit in Fig. 3, considering full models for the varactor diodes and linear components, as in Section III-A. Note that this is different from [32], where the main study was carried out under ideal models. As gathered from (29), to enhance the nonreciprocal behavior, we should maximize the difference between the coefficients $A_{i,f}$ and $A_{i,b}$. Fig. 6 presents the variation of the magnitudes of these two coefficients versus the transmission-line length l [RO4003C ($h = 32$ mil) substrate]. From the inspection of the figure, we can expect a pronounced nonreciprocal behavior about $l \cong 65$ mm.

In Fig. 7(a), we present the power-transfer curves obtained for the transmission-line length: $l = 60$ mm. We indicate with “S” (“U”) the sections with a stable (unstable) behavior. As expected, for too low P_{in} , the behavior is reciprocal, with a very low power transfer. Then, as P_{in} increases, the backward

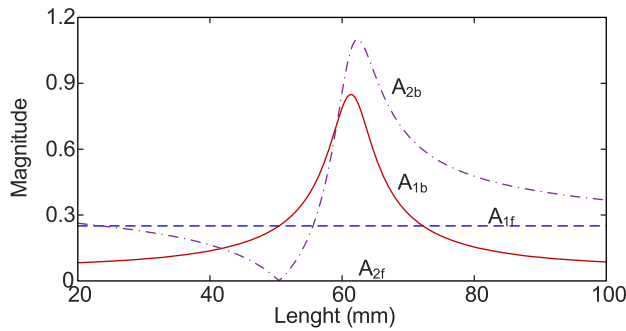


Fig. 6. Variation of the magnitudes of $A_{i,f}$ and $A_{i,b}$ versus the transmission-line length l . The biggest differences are obtained about $l \cong 65$ mm.

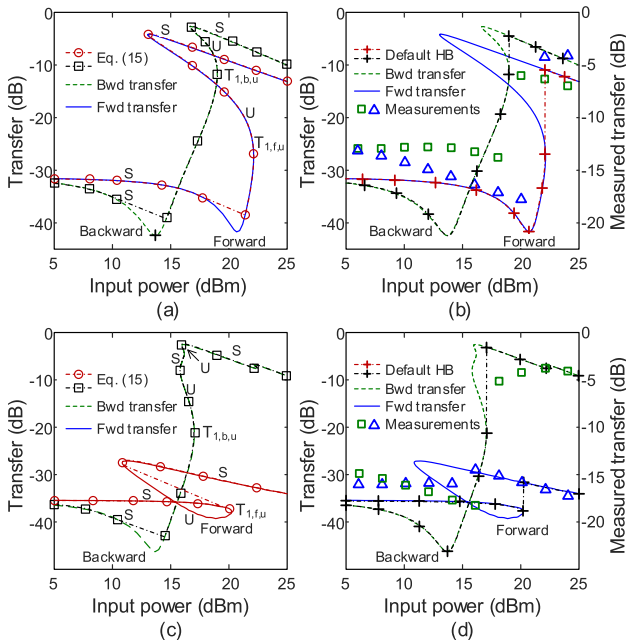


Fig. 7. Analysis of the Lorentzian-Fano nonlinear isolator versus the input power P_{in} for two distinct values of the transmission-line length. (a) $l = 60$ mm. Comparison with the method in [32], which gives rise to some failures in the low power-transfer region. (b) $l = 60$ mm. Comparison with default HB (black dashed-dotted line), unable to complete the curves. Experimental results are superimposed. (c) $l = 70$ mm. Comparison with the method presented in [32], which gives rise to some failures in the low power-transfer region. (d) $l = 70$ mm. Comparison with default HB (black dashed-dotted line), unable to complete the curves. Experimental results are superimposed.

curve starts to grow and undergoes the turning point $T_{1,b,u}$. In the forward sense, the power transfer keeps low up to the turning point $T_{1,f,u}$. The occurrence of $T_{1,b,u}$ before $T_{1,f,u}$ can be related to the larger values of $|A_{i,b}|$ in comparison with $|A_{i,f}|$ observed in Fig. 6 for this length value. To obtain the solution curves through (8), we have used a sweep in phase from 0° to 360° , with a 3° step (121 pts), and a sweep in $|V_{AG2}|$ from 0.001 to 8 V, with a 0.05 V step (161 pts). This double sweep, which takes 33 s in an i9-9940X (32 GB RAM), is carried out at each $|I_g|$ step.

In Fig. 7(a), we compare the results of the new formulation with the method in [32], unable to predict the sections with low power transfer. In the formulation [32], instead of connecting AG2 in parallel with NL2, we connect it in parallel with the series branch NL2- L_2 (see Fig. 3). Thus, the nonlinear element NL2 in the second resonator is not directly excited

across its terminals. This gives rise to convergence problems when the voltage amplitude across the branch NL2- L_2 is small while having a large voltage amplitude across NL2. We must emphasize that if convergence is achieved during the variable sweeps, the result is fully correct (not approximate). In Fig. 7(b), we compare the results of the new formulation with default HB, unable to complete the solution curves. The circuit has also been experimentally characterized and the measurement points are superimposed in Fig. 7(b).

We have performed systematic analyses versus the length l and the difference between $T_{1,f,u}$ and $T_{1,b,u}$ is always relatively small. However, the power transfer after $T_{1,b,u}$ can be rather low for some l values, which will lead to a long P_{in} interval with nonreciprocal behavior. This is shown in Fig. 7(c) and (d), corresponding to $l = 70$ mm. After $T_{1,f,u}$, the saturated voltage values in NL2 keep near those ideally fulfilling $V_2 + jL_2\omega I_2(V_2, \omega) = 0$, so the output power is very low. Another advantage is the sharp transition from low power transmission to high power transmission in the backward sense, instead of the gradual one observed in Fig. 7(a) and (b). Thus, we obtain a quite noticeable nonreciprocal behavior. Note that the transmission loss could be reduced with low-parasitic devices. Fig. 7(c) compares the results of the new formulation with those of [32], which is unable to predict the low amplitude loop. Comparisons with default HB, unable to complete the solution curves, and with measurements are presented in Fig. 7(d).

Fig. 8 presents the analysis versus the input frequency ω at the constant input power $P_{in} = 18$ dBm. For the two length values, $l = 60$ and 70 mm, the solution curves are extremely complex. Moreover, for $l = 60$ mm [Fig. 8(a)], both in the forward and backward senses, there are isolated closed curves, detected in this kind of system for the first time to our knowledge. To better understand the behavior in forward sense, we have also traced the solution curves in terms of the voltage V_2 [Fig. 8(b)]. The existence of the closed curve has been validated through the optimization of the two AGs, in terms of their amplitude and phases, to simultaneously fulfill the two nonperturbation conditions $Y_{AG1} = I_{AG1}/V_{AG1} = 0$ and $Y_{AG2} = I_{AG2}/V_{AG2} = 0$. Convergence of this optimization procedure has only been achieved at two points, indicated with asterisks. With respect to in-house software, relying on continuation techniques, the new method has the advantage of exhaustively providing all the coexistent solutions, which may belong to solution curves that would otherwise be ignored. The isolated curves are missed when AG2 is connected in parallel with the series branch (composed by the inductor L_2 and the diodes D3 and D4), as in [32]. This is because they are caused by the nonlinear behavior of the diodes when the voltage amplitude of the series branch is small. When connected in parallel with the series branch, AG2 is not able to properly excite the diodes.

For $l = 70$ mm [Fig. 8(c)], the frequency interval with low power transfer in the forward sense is broader than the one obtained for $l = 60$ mm. We indicate with "S" the stable section of the lower part of the curve in forward sense. A better operation is obtained for $l = 70$ mm both versus input frequency and power.

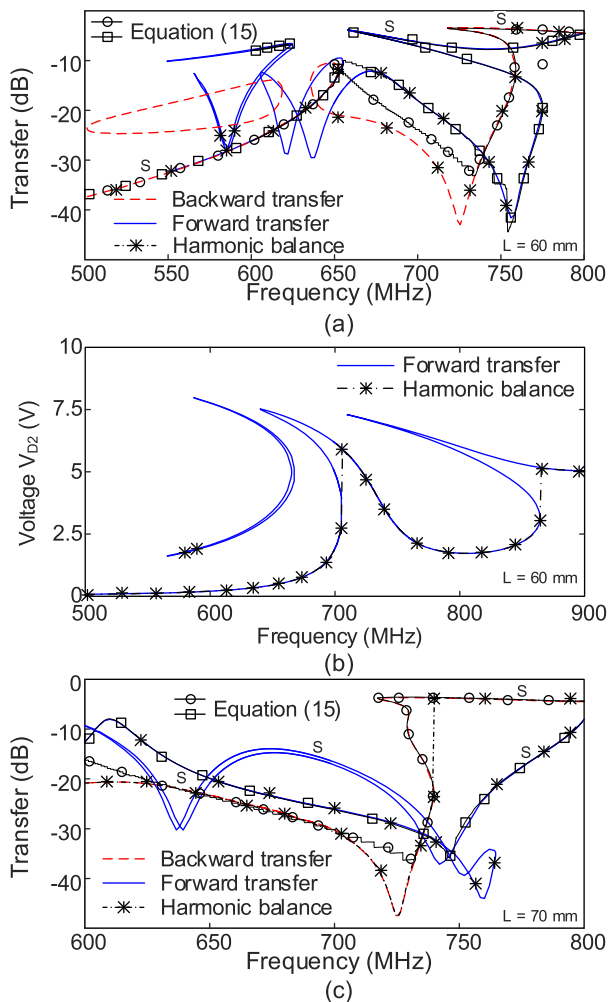


Fig. 8. Analysis of the Lorentzian-Fano nonlinear isolator versus the input frequency ω for two distinct values of the transmission-line length. Comparison with default HB (black dashed-dotted line), unable to complete the curves, and with the method presented in [32], which gives rise to some failures in the low power-transfer region. The existence of the isolated closed curves has been verified through AG optimization (asterisks). (a) $l = 60$ mm. (b) $l = 60$ mm. Solution curve(s) in terms of the voltage V_2 , to better understand the behavior. (c) $l = 70$ mm. The stable section of the lower part of the curve in forward sense is indicated with “S” in (c).

IV. WIRELESS POWER TRANSFER SYSTEM BASED ON TWO COUPLED NONLINEAR RESONATORS

In this section, we will address the wireless-power-transfer system based on two coupled nonlinear resonators proposed in [24] and [25]. The topology is shown in Fig. 9. It can be seen as a significant evolution/improvement of the one proposed in [41] and [42], which contained a single nonlinear resonator in the secondary.

In the system of Fig. 9, we can take the voltage across the pair of diodes in the first (second) resonator as the variable V_1 (V_2). When doing so, we properly excite both NL1 and NL2 and have $A_2 = 0$, so the system can be formulated as in the particular case (13), which corresponds to the method in [32]. As already stated, this formulation is computationally more efficient since the solution curves are obtained through contour plots instead of contour intersections.

For an intuitive understanding, we will also derive a simplified analytical formulation, assuming $L_1 = L_2 = L$ and

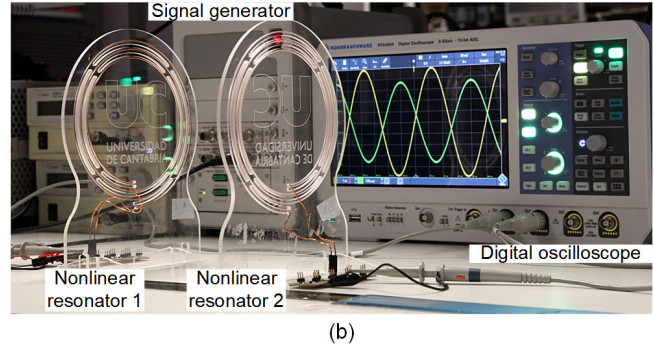
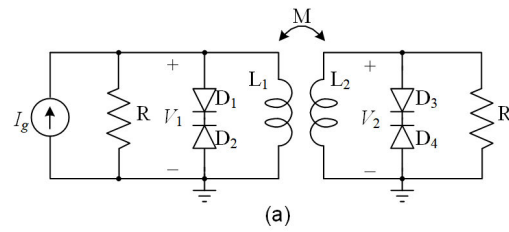


Fig. 9. Robust wireless-power-transfer system based on two nonlinear resonators [24], [25]. (a) Schematic. (b) Photograph of the measurement setup.

expressing the nonlinear currents through NL1 and NL2 in terms of the nonlinear charges. The admittance matrix $[Y_a]$ is given by

$$[Y_a] = \begin{bmatrix} \frac{-j}{(-k^2 + 1)L\omega} + G & \frac{j}{(-k^2 + 1)L\omega} \\ \frac{j}{(-k^2 + 1)L\omega} & \frac{-j}{(-k^2 + 1)L\omega} + G \end{bmatrix} \quad (32)$$

where k is the coupling factor. Replacing $[Y_a]$ in (13), the system equations are

$$\begin{aligned} & \left(\frac{-j}{(-k^2 + 1)L\omega} + G \right) V_1 + j\omega Q_1(V_1) \\ & = I_g - \frac{jk}{(-k^2 + 1)L\omega} V_2(a) \\ & \left(\frac{-j}{(-k^2 + 1)L\omega} + G \right) V_2 + j\omega Q_2(V_2) \\ & = -\frac{jk}{(-k^2 + 1)L\omega} V_1(b). \end{aligned} \quad (33)$$

Under $k = 0$, (33)(a) degenerates into an isolated nonlinear resonator, composed by L , Q_1 , and G , excited by the current I_g . In turn, the resonator in (33)(b), composed by L , Q_2 , and G , becomes undriven, so it provides $V_2 = 0$. For $k > 0$, the second resonator receives (due to the inductive coupling) an input signal from the first one. To perform some more analytical derivations, we will assume identical nonlinear charges, given by $q(t) = C_o v(t)/2 + q_3 v^3(t)$, which provide the describing function: $Q(V) = (C_o/2)V + (3/4)q_3 V^3 = CV + Q_3 V^3$. Now, we will replace these charge functions in (33). Solving for V_1 from (33)(b) (as done with the substitution method) provides

$$V_1 = \frac{1}{k} \left\{ \left[(k^2 - 1)LC\omega^2 + 1 \right] V_2 + (k^2 - 1)LQ_3\omega^2 V_2^3 \right\}. \quad (34)$$

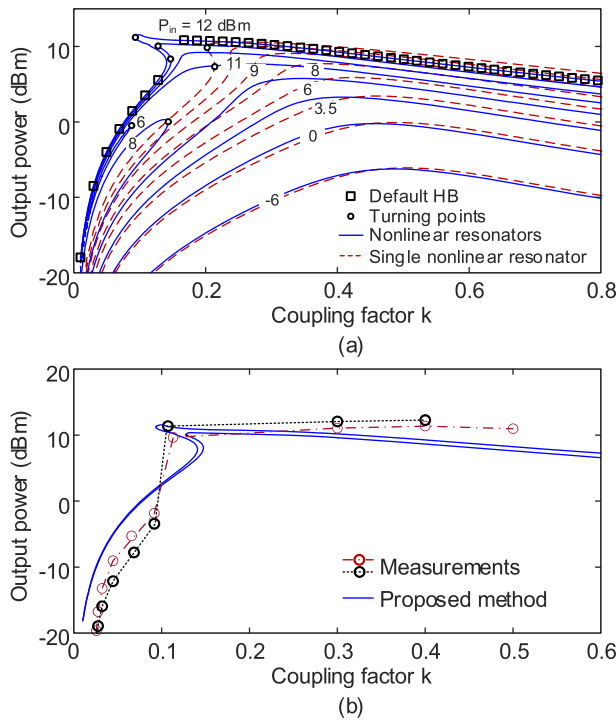


Fig. 10. Transferred power versus the coupling factor k obtained with (35). Solution points obtained with default HB are superimposed with squares. (a) Input frequency $f_{in} = 10$ MHz and different input powers. Comparison of the behavior of the system based on two nonlinear resonators with the one having a single nonlinear resonator in the secondary (case in [41] and [42]). (b) $P_{in} = 10$ dBm, with $f_{in} = 10$ and 11 MHz. The simulations are compared with the experimental results.

As can be seen, one obtains a complex polynomial. When replacing this expression in (33)(a), the complex polynomial is of ninth order. In the case of a linear resonator in the primary, the polynomial keeps of third order of V_1 in (34). As a result, in the case of two nonlinear resonators, we can expect an earlier occurrence of turning points, due to the stronger nonlinearity. This will be verified with the analysis method described in Section II. In this case, we have $A_2 = 0$, so at the fundamental frequency, the system can be compacted as

$$F(|V_2|, k) + A_1(k)|I_g|e^{j\phi} = 0 \quad (35)$$

where the phase origin is set at V_2 . Then, performing a double sweep in k and $|V_2|$, it will be possible to obtain a complete family of solution curves (for different $|I_g|$ values) as contour levels of the function $|H_p| = |F(V_2)/A_1|$. This can be seen in Fig. 10(a), where these contours have been represented, for $f_{in} = 10$ MHz, in the plane defined by k and the output power, given by $P_{out} = (1/2)|V_2|^2/R$. The results are compared with those obtained when having a single nonlinear element, placed in the secondary, which is the case considered in [37] and [38]. As can be seen, with two nonlinear elements, we obtain an earlier saturation and a wider k interval with a low sensitivity. In a manner like what was observed in Section III, for a certain P_{in} interval [see $P_{in} = 6$ and 8 dBm in Fig. 10(a)], there are two isolated curves, which, as shown here, is a common type of behavior in the presence of two nonlinear resonators.

In Fig. 10(b), we compare the simulations of the system with two nonlinear resonators with the measured results for two

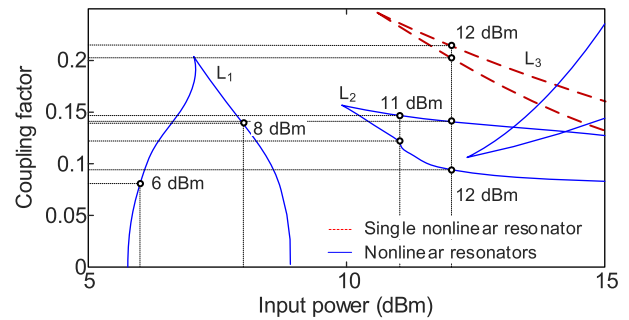


Fig. 11. Locus of turning points in the plane defined by the coupling factor k and the input power P_{in} . It has been obtained from the condition $\partial(|F|^2)/\partial V_2 = 0$, interpolating the P_{in} values that give rise to the zeroes of the derivative function.

different input frequencies $f_{in} = 10$ and 11 MHz. The coupling factor k has been estimated in an empirical manner. We have used the vector network analyzer Copper Mountain S5048 to measure the scattering parameters of a two-port network that included the two coupled coils at different distance values. For each distance d , a set of S -parameters was obtained. The experimental S -parameters were compared with those obtained through the simulation of two mutually coupled ideal inductors for different values of the coupling factor k . The main source of error comes from the fact that planar spiral coils are used in the experiment, whereas ideal inductors are considered in simulation. As seen in Fig. 10(b), the early saturation and jump resulting from the lower turning point are well predicted.

The overall behavior is more regular than the one obtained in the case of the nonlinear isolator. Thus, obtaining the locus of turning points can be helpful for a global prediction of the circuit response. The aim is to trace this locus in the plane defined by P_{in} and k , which will provide, for each P_{in} , the k value at which the upward jump takes place. Through a derivation analogous to the one in (23)–(26), we obtain the turning-point condition $\partial(|F|^2)/\partial V_2 = 0$. To determine the locus in the plane (P_{in}, k) , we will perform a double sweep in k and V and calculate the zero-value contour $\partial(|F|^2)/\partial V_2 = 0$. Then, we will interpolate P_{in} through this contour. The results are shown in Fig. 11, which compares the turning-point loci obtained for two nonlinear resonators (blue solid line) and for a single nonlinear resonator (red dashed line). The loci accurately predict the turning points in the power-transfer curves of Fig. 10(a), as easily gathered by following the vertical axes. In the case of two nonlinear resonators, we obtained three disconnected loci. The locus L_1 in the lower P_{in} range predicts the turning points in the low amplitude curves of Fig. 10(a), without practical interest. The locus L_2 (to be compared with the one obtained with a single nonlinear resonator) demonstrates a general reduction of the k value at which the upward jump (leading to a high power transfer) is obtained.

The circuit has also been analyzed versus the input frequency ω . For $P_{in} = 10$ dBm and different k values, we obtain the results in Fig. 12. Again, the performance of the system with two nonlinear resonators [Fig. 12(a)] is compared with that of the system with a single nonlinear resonator [Fig. 12(b)]. The results obtained with default HB (unable to complete the curves) are superimposed with squares.

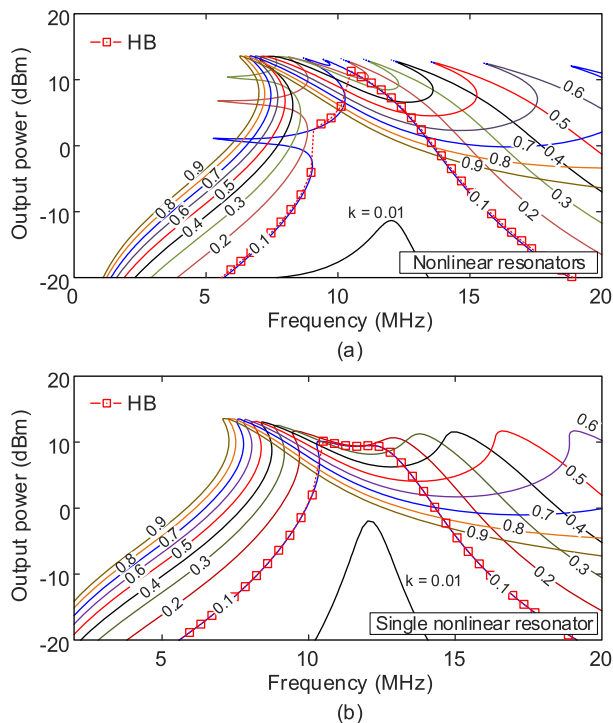


Fig. 12. Analysis versus the input frequency at the input power $P_{in} = 10$ dBm. Solution curves versus the input frequency ω for different values of the coupling factor k . The results obtained with default HB are superimposed with squares. (a) With two nonlinear resonators. (b) With a single nonlinear resonator.

When convergence is achieved, they are overlapped with the ones obtained with the new method. As can be seen, the curves with two nonlinear resonators are significantly more complex than the ones obtained with one nonlinear resonator. Their turning points give rise to jumps and hysteresis when varying the input frequency. At a constant input frequency, their occurrence for low k is what enables the jumps versus P_{in} that lead to a high transferred power [see Fig. 10(a)].

V. CONCLUSION

An exhaustive analysis method for circuits/systems containing two independent nonlinear resonators has been presented. The method is based on a substitution procedure that makes use of two AGs. One of these AGs (AG2) is independent, whereas the other AG (AG1) depends on the AG2 voltage and the input generator. This additional dependence generalizes the analysis of previous work and enables a systematic and broad-scope application, as demonstrated by a rigorous derivation that departs from a piecewise-type HB formulation. The new method is compatible with the use of commercial HB. With respect to in-house HB software combined with continuation techniques, it has the advantage of exhaustively providing all the coexistent solution curves. As another advantage, the method provides insight into the behavior of circuits with a complex performance. Here, it has been applied to a Lorentzian–Fano nonlinear isolator and a robust wireless power-transfer system containing two nonlinear resonators. The results have been compared with default HB and with measurements.

REFERENCES

- [1] X. Zou, Y. Yang, U. Yaqoob, A. Shamim, K. N. Salama, and H. Fariborzi, “A mechanical memory with capacitance modulation of nonlinear resonance,” *IEEE Electron Device Lett.*, vol. 44, no. 6, pp. 923–926, Jun. 2023.
- [2] A. Suárez, R. Melville, and F. Ramírez, “Analysis and synthesis of hysteresis loops in an oscillator frequency characteristic,” *IEEE Trans. Microw. Theory Techn.*, vol. 67, no. 12, pp. 4890–4904, Dec. 2019.
- [3] J. Filip, A. Suárez, and Z. Škvor, “On the stability of oscillatory modes in an oscillator based on a distributed amplifier,” *IEEE Trans. Microw. Theory Techn.*, vol. 71, no. 6, pp. 2422–2438, Jun. 2023.
- [4] V. Ardila, F. Ramirez, and A. Suárez, “Analysis and design of injection-locked oscillators coupled to an external resonator,” *IEEE Trans. Microw. Theory Techn.*, vol. 71, no. 10, pp. 4546–4561, Oct. 2023, doi: 10.1109/TMTT.2023.3259223.
- [5] C. Valagiannopoulos, “Multistability in coupled nonlinear metasurfaces,” *IEEE Trans. Antennas Propag.*, vol. 70, no. 7, pp. 5534–5540, Jul. 2022.
- [6] M. R. E. U. Shougat and S. Ramakrishnan, “The hysteresis phenomenon and q factor enhancement in nonlinear NEMS resonators driven by Lévy stable stochastic processes,” in *Proc. IEEE 13th Nanotechnol. Mater. Devices Conf. (NMDC)*, Portland, OR, USA, Oct. 2018, pp. 1–4.
- [7] O. Shoshani, M. I. Dykman, and S. W. Shaw, “Tuning linear and nonlinear characteristics of a resonator via nonlinear interaction with a secondary resonator,” *Nonlinear Dyn.*, vol. 99, no. 1, pp. 433–443, Jan. 2020.
- [8] R. Quere, E. Ngoya, M. Camiade, A. Suarez, M. Hessane, and J. Obregon, “Large signal design of broadband monolithic microwave frequency dividers and phase-locked oscillators,” *IEEE Trans. Microw. Theory Techn.*, vol. 41, no. 11, pp. 1928–1938, Nov. 1993.
- [9] V. Rizzoli and A. Neri, “State of the art and present trends in nonlinear microwave CAD techniques,” *IEEE Trans. Microw. Theory Techn.*, vol. 36, no. 2, pp. 343–365, Feb. 1988.
- [10] A. Suárez, *Analysis and Design of Autonomous Microwave Circuits*. Hoboken, NJ, USA: Wiley, 2009.
- [11] L. O. Chua and A. Ushida, “A switching-parameter algorithm for finding multiple solutions of nonlinear resistive circuits,” *Int. J. Circuit Theory Appl.*, vol. 4, no. 3, pp. 215–239, Jul. 1976.
- [12] H. G. Brachtendorf, R. Melville, P. Feldmann, S. Lampe, and R. Laur, “Homotopy method for finding the steady states of oscillators,” *IEEE Trans. Comput.-Aided Design Integr. Circuits Syst.*, vol. 33, no. 6, pp. 867–878, Jun. 2014.
- [13] S. Jeon, A. Suarez, and D. B. Rutledge, “Analysis and elimination of hysteresis and noisy precursors in power amplifiers,” *IEEE Trans. Microw. Theory Techn.*, vol. 54, no. 3, pp. 1096–1106, Mar. 2006.
- [14] V. Ardila, F. Ramírez, and A. Suárez, “Nonlinear analysis of a high-power oscillator inductively coupled to an external resonator,” *IEEE Microw. Wireless Compon. Lett.*, vol. 31, no. 6, pp. 737–740, Jun. 2021.
- [15] A. Suarez, J. Morales, and R. Quere, “Synchronization analysis of autonomous microwave circuits using new global-stability analysis tools,” *IEEE Trans. Microw. Theory Techn.*, vol. 46, no. 5, pp. 494–504, May 1998.
- [16] V. Ardila, F. Ramírez, and A. Suárez, “Analytical and numerical bifurcation analysis of circuits based on nonlinear resonators,” *IEEE Trans. Microw. Theory Techn.*, vol. 69, no. 10, pp. 4392–4405, Oct. 2021.
- [17] V. Ardila, F. Ramírez, and A. Suárez, “Nonlinear analysis of an injection-locked oscillator coupled to an external resonator,” *IEEE Microw. Wireless Compon. Lett.*, vol. 32, no. 6, pp. 740–743, Jun. 2022.
- [18] S. Hernández, M. Pontón, and A. Suárez, “Simulation method for complex multivalued curves in injection-locked oscillators,” *IEEE Trans. Microw. Theory Techn.*, vol. 65, no. 11, pp. 4046–4062, Nov. 2017.
- [19] D. L. Sounas, J. Soric, and A. Alù, “Broadband passive isolators based on coupled nonlinear resonances,” *Nature Electron.*, vol. 1, no. 2, pp. 113–119, Feb. 2018.
- [20] M. Cotrufo, S. A. Mann, H. Moussa, and A. Alù, “Nonlinearity-induced Nonreciprocity—Part II,” *IEEE Trans. Microw. Theory Techn.*, vol. 69, no. 8, pp. 3584–3597, Aug. 2021.
- [21] D. L. Sounas and A. Alù, “Nonreciprocity based on nonlinear resonances,” *IEEE Antennas Wireless Propag. Lett.*, vol. 17, no. 11, pp. 1958–1962, Nov. 2018.
- [22] A. Kord, D. L. Sounas, and A. Alù, “Microwave nonreciprocity,” *Proc. IEEE*, vol. 108, no. 10, pp. 1728–1758, Oct. 2020.
- [23] M. Cotrufo, S. A. Mann, H. Moussa, and A. Alù, “Nonlinearity-induced nonreciprocity—Part II,” *IEEE Trans. Microw. Theory Techn.*, vol. 69, no. 8, pp. 3584–3597, Aug. 2021.

- [24] X. Wang and A. Mortazawi, "Bandwidth enhancement of RF resonators using duffing nonlinear resonance for wireless power applications," *IEEE Trans. Microw. Theory Techn.*, vol. 64, no. 11, pp. 3695–3702, Nov. 2016.
- [25] O. Abdelatty, X. Wang, and A. Mortazawi, "Position-insensitive wireless power transfer based on nonlinear resonant circuits," *IEEE Trans. Microw. Theory Techn.*, vol. 67, no. 9, pp. 3844–3855, Sep. 2019.
- [26] M. Pandit, C. Zhao, G. Sobreviela, S. Du, X. Zou, and A. Seshia, "Utilizing energy localization in weakly coupled nonlinear resonators for sensing applications," *J. Microelectromech. Syst.*, vol. 28, no. 2, pp. 182–188, Apr. 2019.
- [27] M. Pandit, C. Zhao, G. Sobreviela, A. Mustafazade, and A. A. Seshia, "Coupled nonlinear MEMS resonators for sensing," in *Proc. IEEE Int. Freq. Control Symp. (IFCS)*, May 2018, pp. 1–4.
- [28] T. Ikehashi, H. Maekoba, and A. Parent, "Characterization of nonlinear behavior of weakly coupled resonators based on nonlinearity factor," *IEEE Sensors J.*, vol. 21, no. 21, pp. 24226–24237, Nov. 2021.
- [29] V. Pachkawade, "State-of-the-art in mode-localized MEMS coupled resonant sensors: A comprehensive review," *IEEE Sensors J.*, vol. 21, no. 7, pp. 8751–8779, Apr. 2021.
- [30] T. Rabenimanana, V. Walter, N. Kacem, P. L. Moal, and J. Lardiès, "Nonlinear analytical model of two weakly coupled MEMS cantilevers for mass sensing using electrostatic actuation," *Proceedings*, vol. 2, no. 13, p. 1084, Nov. 2018.
- [31] M. Lyu et al., "Nonlinearity modulation in a mode-localized mass sensor based on electrostatically coupled resonators under primary and superharmonic resonances," *Phys. Scripta*, vol. 98, no. 4, Apr. 2023, Art. no. 045217.
- [32] A. Suárez and F. Ramírez, "Substitution method for the analysis of systems based on two nonlinear resonators," *IEEE Microw. Wireless Technol. Lett.*, vol. 33, no. 6, pp. 787–790, Jun. 2023.
- [33] S. Mons, R. Quere, T. Peyretailade, and J. Obregon, "Nonlinear stability analysis of MMIC power amplifiers," in *Proc. 28th Eur. Microw. Conf.*, Amsterdam, The Netherlands, Oct. 1998, pp. 114–118.
- [34] S. Mons, M. A. Perez, R. Quere, and J. Obregon, "A unified approach for the linear and nonlinear stability analysis of microwave circuits using commercially available tools," in *IEEE MTT-S Int. Microw. Symp. Dig.*, Anaheim, CA, USA, Oct. 1999, pp. 993–996.
- [35] S. Mons, J.-C. Nallatamby, R. Quere, P. Savary, and J. Obregon, "A unified approach for the linear and nonlinear stability analysis of microwave circuits using commercially available tools," *IEEE Trans. Microw. Theory Techn.*, vol. 47, no. 12, pp. 2403–2409, Dec. 1999.
- [36] R. C. Melville and A. Suárez, "Experimental investigation of bifurcation behavior in nonlinear microwave circuits," *IEEE Trans. Microw. Theory Techn.*, vol. 65, no. 5, pp. 1545–1559, May 2017.
- [37] F. Ramirez, M. E. de Cos, and A. Suarez, "Nonlinear analysis tools for the optimized design of harmonic-injection dividers," *IEEE Trans. Microw. Theory Techn.*, vol. 51, no. 6, pp. 1752–1762, Jun. 2003.
- [38] J. de Cos, A. Suarez, and F. Ramirez, "Analysis of oscillation modes in free-running ring oscillators," *IEEE Trans. Microw. Theory Techn.*, vol. 60, no. 10, pp. 3137–3150, Oct. 2012.
- [39] J. Jugo, J. Portilla, A. Anakabe, A. Suárez, and J. M. Collantes, "Closed-loop stability analysis of microwave amplifiers," *Electron. Lett.*, vol. 37, no. 4, p. 226, 2001.
- [40] J.-M. Collantes et al., "Pole-zero identification: Unveiling the critical dynamics of microwave circuits beyond stability analysis," *IEEE Microw. Mag.*, vol. 20, no. 7, pp. 36–54, Jul. 2019.
- [41] R. Chai and A. Mortazawi, "A position-insensitive wireless power transfer system employing coupled nonlinear resonators," *IEEE Trans. Microw. Theory Techn.*, vol. 69, no. 3, pp. 1752–1759, Mar. 2021.
- [42] R. Chai and A. Mortazawi, "A new coupling insensitive nonlinear capacitive resonant wireless power transfer circuit," in *Proc. IEEE Wireless Power Transf. Conf. (WPTC)*, San Diego, CA, USA, Jun. 2021, pp. 1–4.



Almudena Suárez (Fellow, IEEE) was born in Santander, Spain. She received the Licentiate degree in electronic physics and the Ph.D. degree from the University of Cantabria, Santander, in 1987 and 1992, respectively, and the Ph.D. degree in electronics from the University of Limoges, Limoges, France, in 1993.

She has authored the book *Analysis and Design of Autonomous Microwave Circuits* (IEEE-Wiley, 2009) and coauthored the book *Stability Analysis of Nonlinear Microwave Circuits* (Artech House, 2003).

Prof. Suárez was a member of the Board of Directors of European Microwave Association (EuMA) from 2012 to 2020. She is a member of the TPRCs of IEEE International Microwave Symposium and European Microwave Week. She received the Research Award of the Social Council of the University of Cantabria in 2021. She was an IEEE Distinguished Microwave Lecturer from 2006 to 2008. She was the Coordinator of the Communications and Electronic Technology Area for the Spanish National Evaluation and Foresight Agency (ANEP) from 2009 to 2013. She has been the Publication Officer of EuMA since 2021. She was the Chair of the 2014 and 2015 Editions of IEEE Topical Conference on RF/Microwave Power Amplifiers (PAWR), in Newport Beach and San Diego. She was the General TPC Chair of EuMW 2018. She was the Chair of the IEEE Subcommittee for the Best Paper Award in *IEEE Microwave Magazine* from 2017 to 2022. She was the Editor-in-Chief of the *International Journal of Microwave and Wireless Technologies* of Cambridge University Press journals from 2013 to 2018 and an Associate Editor of *IEEE Microwave Magazine* from 2014 to 2022. Since October 2022, she has been the Editor-in-Chief of IEEE TRANSACTIONS ON MICROWAVE THEORY AND TECHNIQUES.



Franco Ramírez (Senior Member, IEEE) received the Licentiate degree in electronic systems engineering from the Military School of Engineering (EMI), La Paz, Bolivia, in 2000, and the Ph.D. degree in communications engineering from the University of Cantabria, Santander, Spain, in 2005.

From 1999 to 2000, he worked at Ericsson de Bolivia Telecomunicaciones, La Paz, where he was involved in projects related to global system for mobile communications (GSM) and time-division multiple access (TDMA) technologies.

From 2009 to 2013, he was a Research Fellow of the "Ramón y Cajal" Program, funded by the Spanish Ministry of Science and Innovation, at the Communications Engineering Department, University of Cantabria, where he is currently an Associate Professor. His research interests include phase noise, stability, and the development of nonlinear techniques for the analysis and design of autonomous microwave circuits.